Chapter 8

Development of a Comprehensive Process Model for Hybrid Laser-Arc Welding

Fanrong Kong and Radovan Kovacevic

Additional information is available at the end of the chapter

http://dx.doi.org/10.5772/45850

1. Introduction

Recently, a hybrid welding technique combining laser welding and arc welding has been finding broader applications in industry due to its unique advantages, such as higher welding efficiency and lower costs [1, 2] compared to the traditional arc welding or autogenous laser welding. Because of rapid melting and solidification occurring in the weld zone, a locally high thermal gradient inevitably exists and accompanies with the whole welding process, which really decides the final residual stress and distortion distributions of weld and affects the remained grain size in the fusion zone (FZ) and heat affected zone (HAZ). Also, the levels of residual stresses and distortions directly influence the weld quality [3]. In comparison with traditional arc welding and autogenous laser welding, the temperature field and residual stress distribution in hybrid laser-arc welding involve more variables because of the additional interaction between the laser and arc plasma [4] thus becoming much more complex and difficult to theoretically and experimentally analyze. Trial-and-error experiments are not able to fully describe those physical mechanisms involved in the hybrid laser-arc welding process. Therefore, the numerical tools have been widely used to help explain the complex welding mechanisms present in the hybrid laser-arc welding process [5, 6].

Up to now, numerical work on the welding process mostly concentrates on traditional electric arc welding, including gas tungsten arc welding (GTAW) [7 - 9], submerged arc welding (SAW) [10,11], gas metal arc welding (GMAW) [12-16], and partly on laser beam welding (LBW) [17-21]. These studies focused on the heat and mass transfer phenomena in the weld pool [8, 11-15], thermal-induced distortion and residual stresses [16, 17, 19, 20], solidification-induced dendrite growth in the FZ [21], and recrystallization in the heat affected zone (HAZ) [9]. Due to the locally rapid melting and solidification occurring in the welding process, a high temperature gradient—which inevitably exists in the weld zone—

causes a high-stress concentration in the weld zone and nearby HAZ [22], which usually exceeds the yield strength of the material. Large residual stresses presented in the welded structure can obviously reduce the fatigue strength of metal components, causing crack generation and shorten the lifetime of metal component [23], which could possibly have disastrous results. A number of mitigation procedures to reduce and/or eliminate the level of residual stress have been presented by researchers, mainly including enhancement of the material ductility of solidification zone (SZ) and HAZ, and improving the thermal and mechanical conditions in the welding processes [24].

Because of the complex physical mechanisms in the welding process—which are related to the heat source properties, material performance, and welding parameters, etc.—trial-and-error methods to optimize welding parameters takes a long time and is usually more costly. Also, understanding of the physics of the welding process is limited by only using an experimental approach. Numerical simulation as accompanied by theoretical analysis has been widely applied as a cost-efficient way to help explore the welding phenomena in different welding techniques. Eagar et al. [25, 26] spent a lot of time in developing theoretical models for GTAW processes. Dong et al. [27-29] developed numerical models to predict the residual stresses as well as fatigue life of weld obtained by the multi-pass welding process. Deng et al. [30-32] developed a series of numerical models to study the residual stress distribution in variable welding joints.

Compared to the traditional electric arc welding, laser welding has unique advantages such as high energy density, narrow HAZ, low heat input, and high energy efficiency. However, laser welding is also limited by its disadvantages like poor gap bridgeability and high equipment cost. In order to fully use the advantages of both laser and arc welding techniques, Steen et al. [33] introduced for the first time a hybrid technique by combining the laser beam and arc for welding and cutting in the late 1970s. Subsequently, researcher and engineers have presented a number of works on combining the laser and electric arc in the past decades. Considering that interaction between laser beam and arc plasma is complex, the hybrid laser-arc welding and cladding processes have not been understood fully. Most available literature on these approaches is limited at the level of the experimental study including hybrid laser-GTAW, hybrid laser-GMAW, and hybrid laser-plasma arc welding for steels, magnesium alloy, aluminum alloy, titanium alloy and dissimilar materials. In order to further study the welding mechanism of hybrid laser and arc, it is necessary to develop a comprehensive model to understand the heat and mass transfer, residual stress evolution, as well as microstructure formation in the hybrid laser-arc welding process. Zhou and Tsai [34, 35] presented heat transfer and fluid flow models to study the metal inert gas (MIG) welding and laser-MIG hybrid welding processes. Rao et al. [36] reviewed the modeling of hybrid laser-gas metal arc (GMA) welding and presented further studies on synergistic interaction between the laser beam and arc, the metal transfer features, and behavior of shielding gas. Ribic et al. [37] developed a three-dimensional (3-D) finite volume model to study heat transfer and fluid flow in the hybrid laser-GTA welding process. Considering that the microstructure formation of weld has a close relationship with the macro-scale heat transfer and fluid flow, and residual stress fields, it will be very

necessary to integrate the thermal, fluid flow and mechanical modeling with the microstructure evolution like grain growth in the fusion zone and HAZ. Multi-scale and multi-physics modeling is one of most interesting simulation trends in the laser-based heat processes, especially in the hybrid laser-arc welding process.

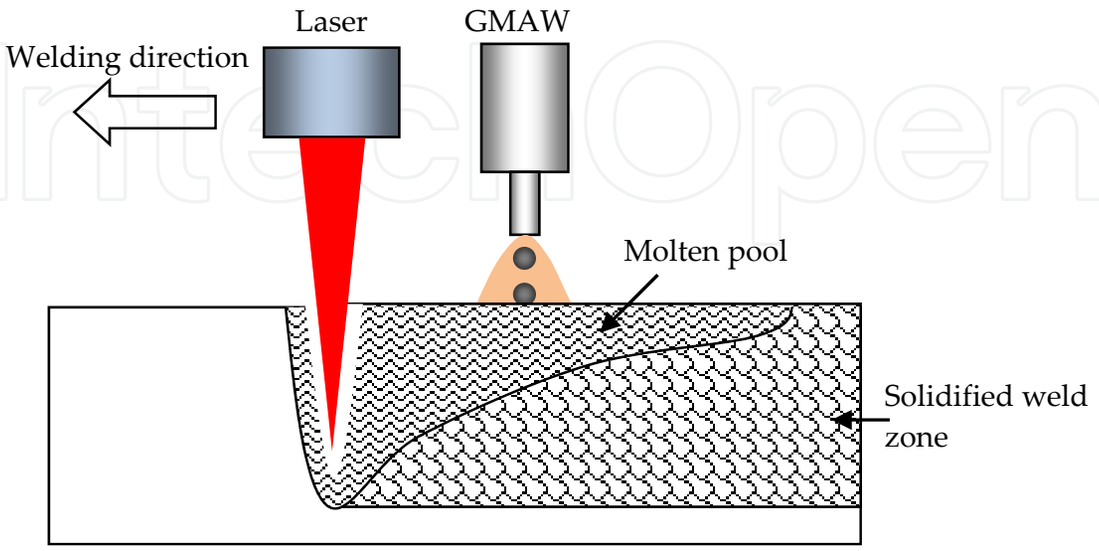

Figure 1. Schematic view of hybrid laser-GMA welding system

In this chapter, a 3-D mathematical model will be developed to numerically predict the transient temperature distributions and residual stresses in the hybrid laser-GMA welding of a thick plate of A514 steel in butt joint configuration, as shown in Figure 1. The numerical solution is achieved based on a finite element method by using a commercial numerical package, ANSYS. A Monte Carlo model is introduced to consider the grain growth and phase transformations in the HAZ. The laser and arc heat inputs and heat losses at the surface of coupons are considered by using ANSYS Parametric Designed Language (APDL). The influences of the processing parameters (including welding speed, laser power, wire feed rate, arc power, and stand-off distance from laser to arc) on the profile and geometrical size of the molten pool, residual stress distribution of the weld, and grain size in the HAZ are numerically studied. The numerically obtained results are experimentally verified.

2. Finite element modeling

2.1. Thermal analysis of hybrid laser-GMA welding

In the hybrid laser-GMA welding process, laser and GMA simultaneously heat the coupon surface in local area, which makes the thermal distribution of weld much more complex. In this study, a cylindrical volume heat-source model with a Gaussian distribution is assumed to simulate the heat input by laser, and a double-ellipsoidal volume heat source is selected to consider the heat input by GMA welding. The general thermal governing equation is shown below, in which thermal conduction-induced heat transfer is considered and temperature-dependent material properties are used [38].

$$\rho c_p \frac{\partial T}{\partial t} = \{L\}^T (\lceil D \rceil \{L\} T) + \ddot{q}_l + \ddot{q}_a \tag{1}$$

$$\text{where} \lceil D \rceil = \begin{bmatrix} k_{xx} & 0 & 0 \\ 0 & k_{yy} & 0 \\ 0 & 0 & k_{zz} \end{bmatrix}, \tag{2}$$

$$\text{and} \{L\} = \begin{Bmatrix} \frac{\partial}{\partial x} \\ \frac{\partial}{\partial y} \\ \frac{\partial}{\partial z} \end{Bmatrix}, \tag{3}$$

ρ is the density, c_p is the specific heat, T is the temperature, t is time, k_{xx}, k_{yy}, and k_{zz} are the thermal conductivity components along the x, y, and z axis, respectively; $\ddot{q}_l$ and $\ddot{q}_a$ are the volume heat generation rates due to the laser and GMA heat input, respectively.

So far, a number of heat source models have been developed to simulate the arc welding and laser welding processes. Laser welding usually consists of laser conduction welding or laser keyhole welding. The former one has lower energy density as compared with the latter one by which a keyhole is formed in the weld pool. A surface heat flux model is usually applied in the thermal analysis of laser conduction welding. However, a volume-distributed heat source model, like rotary Gaussian heat density distribution [39], is usually used for simulating a laser keyhole welding. Compared to the laser beam welding, electric arc welding has much lower energy density, and surface heat flux models with Gaussian distributions used to be applied to simulate the arc heat input in the arc welding process.

Considering that the enthalpy brought into the weld pool by melted wire in GMAW, volume-distributed heat source models are preferred, such as hemi-spherical power density distribution [40], ellipsoidal power density distribution [41], and double ellipsoidal power density distribution [42]. However, all of these heat source models are empirically derived based on the experimentally fitting data. Therefore, each heat source model mentioned above has a certain applicable range in the real production case. It is suggested that engineers in the welding process design should reasonably select a heat source model which matches well with the specific welding process. There are a limited number of publications available to numerically describe the hybrid laser and arc welding process because of lack of knowledge on complex interaction between the material, arc plasma, and laser beam [43]. Current heat source models of hybrid laser and arc including GTAW and GMAW were mostly developed with the help of experimental support [34-37].

In this study, a double-ellipsoidal heat source model is introduced to simulate the GMAW heat input, and a cylindrical heat source model with a sectional Gaussian distribution is used to consider the laser heat input. q^f_{arc} (x, y, z, t) and q^r_{arc} (x, y, z, t), depict heat input distributions inside the front and rear quadrants of the GMAW heat source, respectively, which can be expressed as follows [42, 44]:

$$\dot{q}_{arc}^{f}(x,y,z,t)=\frac{6\sqrt{3}f_f P_{arc}}{abc_f\pi\sqrt{\pi}}\exp\left(-\frac{3(x-x_0)^2}{a^2}\right)\cdot\exp\left(-\frac{3(y-L_w)^2}{b^2}\right)\cdot\exp\left(-\frac{3(z-vt)^2}{c_f^2}\right) \quad (4)$$

$$\dot{q}_{arc}^{r}(x,y,z,t)=\frac{6\sqrt{3}f_r P_{arc}}{abc_r\pi\sqrt{\pi}}\exp\left(-\frac{3(x-x_0)^2}{a^2}\right)\cdot\exp\left(-\frac{3(y-L_w)^2}{b^2}\right)\cdot\exp\left(-\frac{3(z-vt)^2}{c_r^2}\right) \quad (5)$$

where a, b, c_f, c_r are the characteristic parameters of heat sources, and a, b, c_f, and c_r are set at 4 mm, 3 mm, 3 mm and 7 mm respectively [44]. P_{arc} denotes the nominal power of the GMAW, and $P_{arc}=\mu UI$. Where μ is the energy efficiency of GMAW based on the welded metal, U denotes the arc voltage of GMAW, and I stands for arc current of GMAW. $\dot{q}_{laser}(x,y,z,t)$ denotes the laser radiation-induced volume heat input given by [45, 46]:

$$\dot{q}_{laser}(x,y,z,t)=\eta_l\frac{P_{laser}\cos\Phi}{2\pi R_l^2}\exp\left(-\frac{(x-x_0)^2+[z+(L_w-y)\tan\Phi-vt-D_{la}]^2\cos^2\Phi}{2R_l^2}\right) \quad (6)$$
$$\cdot(y/L_w^2)$$

where η_l is laser absorption efficiency based on the welded material, P_{laser} stands for the nominal power of the laser beam, x_0 is the x-coordinate of the center point of laser spot at the coupon surface, L_w is the thickness of the butt joint, and R_l is the effective radius of the laser beam, Φ is the inclination angle of laser head, D_{la} is the laser-to-arc stand-off distance. Φ is set at 0^o and D_{la} is set at 8 mm in this study, and v denotes the welding speed.

The boundary conditions at the sample surfaces are given by:

$$-k\frac{\partial T}{\partial n}=h_c(T-T_\infty) \quad (7)$$

where n is the normal outward vector to the surface of specimen, T_∞ is the room temperature, and h_c is the heat transfer coefficient of sample surface.

2.2. Mechanical analysis of hybrid laser-GMA welding

The mechanical analyses of hybrid laser and arc welding are similar to the previous studies on the electric arc welding and laser welding. The stress and distortion of weld are mainly caused by the thermally-induced expansion and shrinkage and the accompanying phase transformation-induced volume change. By considering the elastic-plastic material properties, stress and strain relationships in the hybrid laser-GMA weld are given by [38]:

$$\{\sigma\}=[D_e]\{\varepsilon^{el}\} \quad (8)$$

where {σ} denotes the stress vector, $[D_e]$ denotes elastic stiffness matrix, and $\{\varepsilon^{el}\}$ denotes elastic strain vector expressed by [30]:

$$\{\varepsilon^{el}\}=\{\varepsilon\}-\{\varepsilon^{th}\}-\{\varepsilon^{pl}\}-\{\varepsilon^{\Delta V}\}-\{\varepsilon^{Trp}\} \quad (9)$$

where $\{\varepsilon\}$ is the total strain vector, $\{\varepsilon^{th}\}$ is thermal strain vector, $\{\varepsilon^{pl}\}$ is the plastic strain vector, $\{\varepsilon^{\Delta V}\}$ is strain vector due to phase transformed induced volume change, and $\{\varepsilon^{Trp}\}$ is strain vector due to phase transformation plasticity which is ignored in this study. The boundary conditions taken into consideration in the mechanical analysis assume that one edge of the butt joint is fixed, and the other one is only transversely shrinkage free.

2.3. Grain size prediction model by Monte Carlo method

Grain size evolution and phase transformation play a critical role in deciding the final mechanical properties of weld, and it is necessary to involve those factors in the thermo-mechanical modeling of different welding processes. Many good trials have been performed to numerically predict the grain growth in the fusion zone and heat affected zone for solidification and re-crystallization, respectively, which includes Monte Carlo (MC) model [47-50], phase field (PF) method [51], and cellular automaton (CA) model [52] combined with finite element and finite difference analyses. Here a brief introduction of MC model to predict the grain growth in HAZ will be performed. The detailed description of phase field method and cellular automaton model-based numerical prediction of grain growth in welds can be found in literature [53].

Monte Carlo model-based grain growth prediction generally includes the following several steps: (1) The representation of the considered material in a two-dimensional (2-D) or 3-D of cells, as shown in Figure 2a. The content of each cell stands for its crystallographic orientation. A region consisting of a set of consistently distributed cells with the same orientation value denotes a grain. The grain boundaries are identified by a curve in 2-D matrix or a surface in 3-D matrix between the separate planes or volumes with different orientations. (2) After selecting the matrix type and defining it by an initially random number, the free energy of a cell in the matrix with its specific crystallographic orientation based on its surroundings will be identified. (3) Randomly selecting a new crystallographic orientation for each cell. (4) Calculating the free energy of the new coming element with the new crystallographic orientation, the two energy values and their difference are then calculated. A new grain orientation that will minimize the free energy is generated with the selected transition probability [54]. These four steps will be reiterated many times at random positions in the matrix. The ultimate product is a microscopic simulation of the free energy decaying in the system, which is in fact the main driving force for grain growth. The Hamiltonian demonstrates the interaction among the closest neighbors in a particular cell, which stands for the grain boundary energy and can be calculated as follows [54]:

$$G = -J\sum_{nn}(\delta s_i s_j - 1) \tag{10}$$

where, J is a positive constant that characterizes the scale of the grain boundary energy; s_i is one of the possible orientations, which is set between 1 and q, in the i^{th} cell of the matrix; s_j is the crystallographic orientation of one neighboring cell; nn is the amount of neighboring cells for each element. In the Monte Carlo model, a Moore neighborhood model is selected

(see Figure 2b); therefore, nn=8. δ_{ab} is the Kronecker-delta, which equals 1 when two elements in the matrix are equal, i.e., a=b, and 0 for others. As a consequence, neighboring cells with different orientations contribute a free energy J to the system and 0 with the same orientation. The total number of grain orientations, q is set at 40 in this model since it is known that the grain-growth exponent becomes almost independent of q when its value is larger than 30 [54].

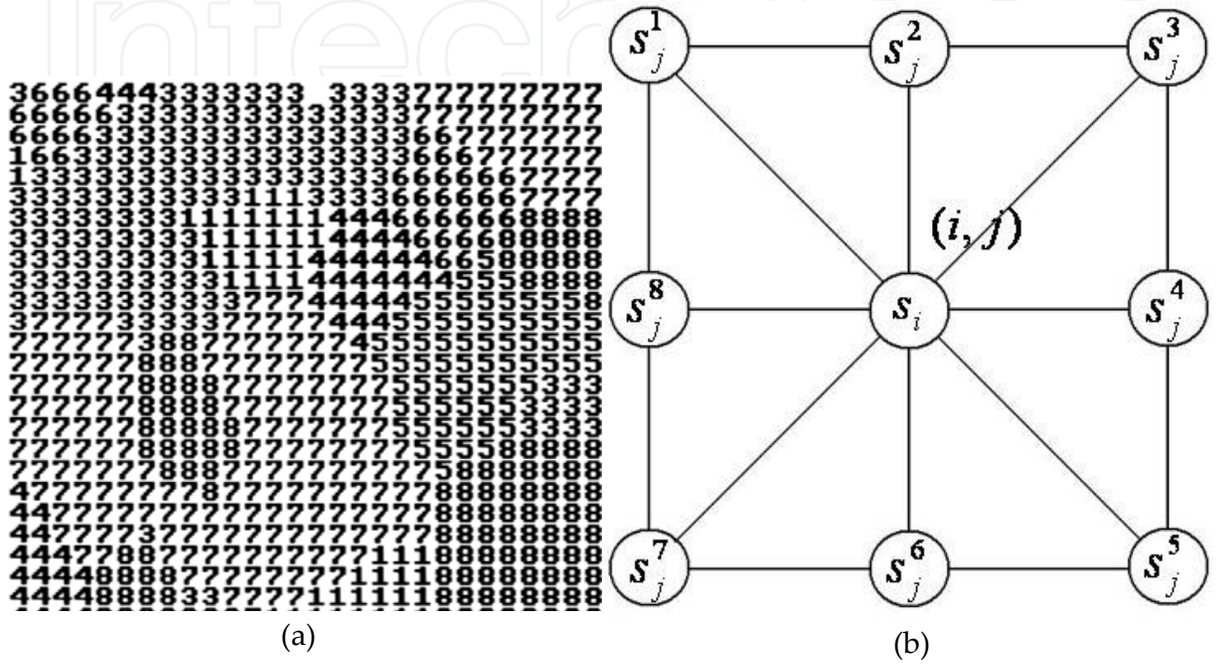

Figure 2. The grain structure in MC model with Moore neighborhood [51]
(a) The grain structure represented by a 2D square (b) Moore neighborhood

The transition probability W is given by [55]:

$$W = \begin{cases} \exp(-\dfrac{\Delta G}{k_b T}), & \Delta G > 0 \\ 1, & \Delta G \le 0 \end{cases} \tag{11}$$

where ΔG is the change of the free energy because of the orientation alteration, k_b is the Boltzman constant (k_b=1.38×10^{-23} m^{2}kg/s^2/K), and T is the temperature. Therefore, the speed of the moving segment can be calculated by [55]:

$$v_i = C_1[1 - \exp(-\frac{\Delta G}{k_b T})] \tag{12}$$

where C_1 is the boundary mobility. For a continuous grain growth, the final grain size can be calculated by using the following equation [55]:

$$L^n - L_0^n = f(T)t \tag{13}$$

where L and L_0 are the final and initial mean grain sizes respectively calculated by the linear-intercept method, n is the grain growth exponent and set at 1.84 in this study [56]. f(T) is usually computed as an Arrhenius-type equation [55], and its expression is shown as follows:

$$f(T) = K\exp(-\frac{Q}{R_g T}) \tag{14}$$

where K is the pre-exponential coefficient, Q is the activation energy for grain growth, and R_g is the universal gas constant. In this study, K is set at 3.01×10^{-2}, and Q is set at 1.7×10^5 J/mol [56].

The Monte Carlo method has been proven to be an effective way to simulate grain growth with slow and uniform temperature evolution such as metal casting [53]. In the hybrid welding by laser and arc, there exists a dynamic thermal process with rapid heating and cooling resulting in an abrupt temperature gradient in the HAZ and fusion zone. In the simulation of microstructure evolution, three techniques—such as the atomistic models, a grain boundary migration (GBM), and experimentally data-based (EDB) models—have been presented [53, 58-60]. The atomistic model used to be only applied to small numbers of atoms like nanocrystals [60], and it is not suitable for a large-scale FZ or HAZ simulation. The GBM model can be a good alternative for grain-growth simulation when the isothermal grain-growth kinetics is not accessible. However, the physical properties of the material in this model have to be known, and the grain size is assumed to be proportional to the square root of time. The EDB model can avoid these shortages and be applied to simulate the grain growth in HAZ when the isothermal grain-growth kinetics of metal are available. Therefore, it can be used to relate time and temperature to the Monte Carlo simulation-time step t_{MCS} [55]:

$$L = K_1\lambda(t_{MCS})^{n_1} \tag{15}$$

where λ is the discrete grid-point spacing in the Monte Carlo model, and K_1 and n_1 are constants. Through the regression computation of t_{MCS} and the Monte Carlo model predicting the grain size, the values of K_1 and n_1 are obtained as 0.715 and 0.477, respectively [56]. In the EDB model, the relationship between the t_{MCS} and the real time-temperature T(t) is further given by [60]:

$$(t_{MCS})^{nn_1} = (\frac{L_0}{K_1\lambda})^n + \frac{K}{(K_1\lambda)^n}\sum(\exp(-\frac{Q}{R_g T(t)})\Delta t_i) \tag{16}$$

where n is the grain growth exponent, T(t) is the mean temperature in a time interval Δt_i. Therefore, at any given monitoring location where the temperature is known as a function of time, t_{MCS} can be related to the real time t, which is $\sum\Delta t_i$. The t_{MCS} values at different locations calculated through Eq. (16) cannot be straightly applied to the Monte Carlo model since the selection of a grid point for updating the orientation number is stochastic in the Monte Carlo approach. Consequently, the probability of choosing each grid point is the

same as in the traditional MC calculations. However, grains usually grow at higher rates in the HAZ region of higher temperature, where a sharp temperature gradient is present. This fact has to be included in any practical grain-growth calculation scheme. One solution is to develop a scheme in which grain orientations at higher-temperature locations (higher t_{MCS} locations) are updated with a higher frequency by considering a probability gradient. In other words, the site-selection probability changes with location. The larger the t_{MCS} at a location, the higher the corresponding site-selection probability [57, 60]:

$$P = t_{MCS} / t_{MCSMAX} \tag{17}$$

where t_{MCSMAX} is the maximum of t_{MCS} in the simulation domain.

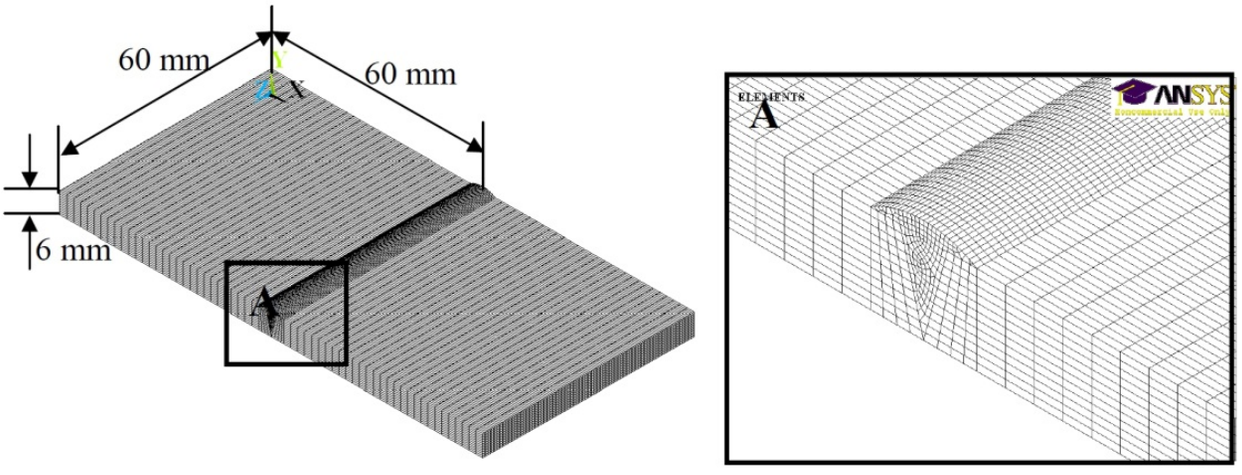

Figure 3. Finite element meshes for hybrid laser-GMA weld

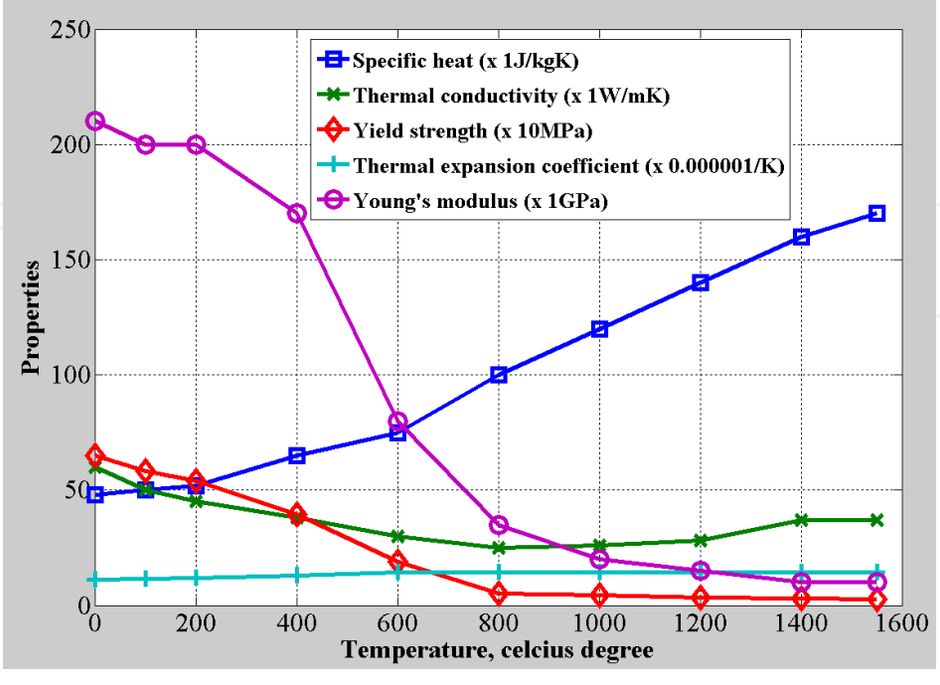

Figure 4. Temperature-dependent thermal and mechanical properties of A514 steel

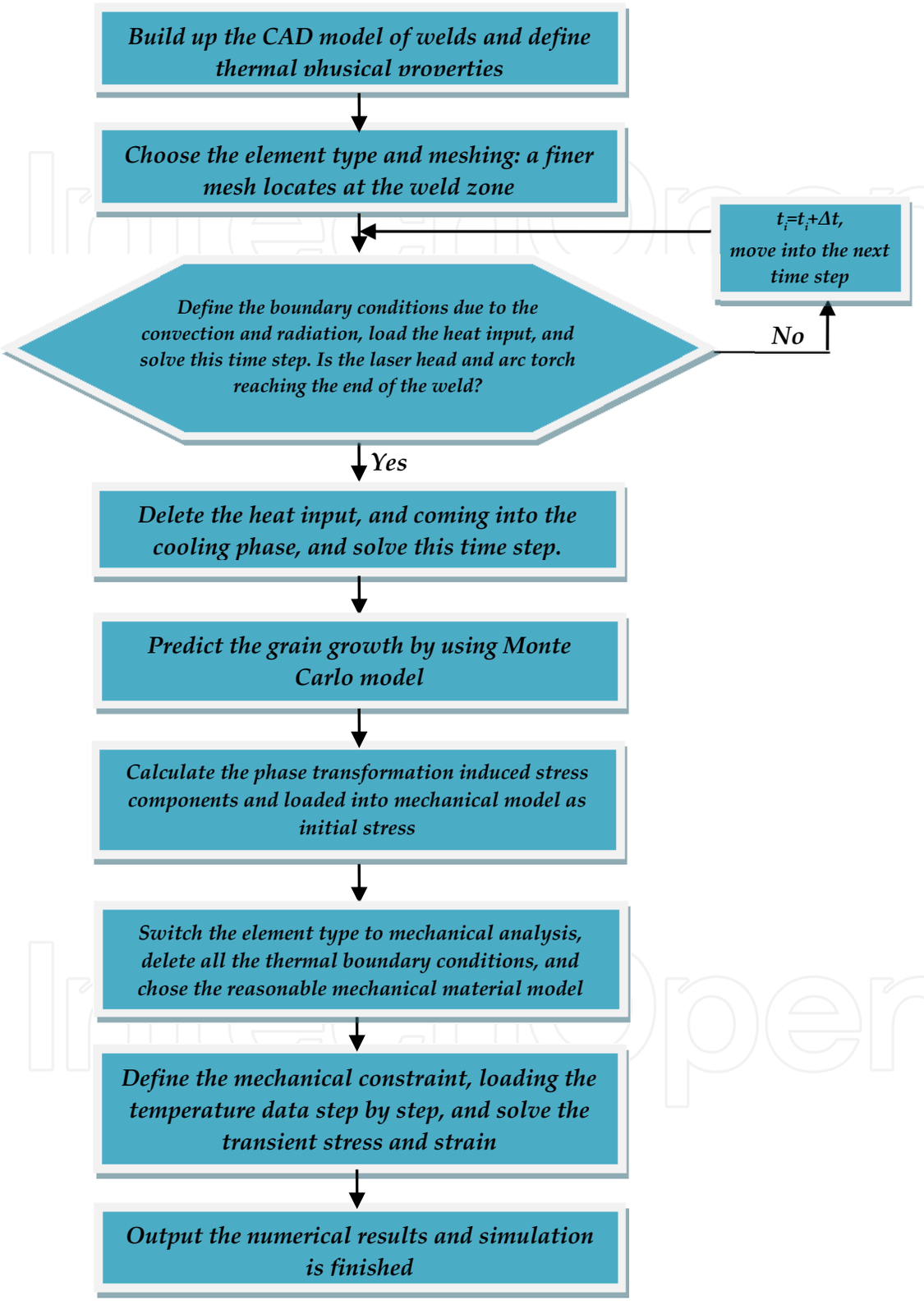

Figure 5. Numerical procedure performed in the thermo-mechanical FE analysis

2.4. Implementation of numerical procedure by using APDL

An uncoupled finite element thermo-mechanical model with considering the grain growth in the HAZ by Monte Carlo model is developed to study the temperature distribution and residual stress field in the hybrid laser-GMA welding process. A non-uniform mesh is selected in which a finer mesh is used in the weld bead and a course mesh is defined in the other region of the welded coupons (see Figure 3). A temperature-dependent material property is used in the numerical modeling, as listed in Figure 4. A thermal FE analysis is performed to achieve the temperature field of hybrid laser-GMA welding process. The wire feeding into the groove to form the weld bead has been simulated by using element kill-and-birth approach which is available in ANSYS software. The achieved geometrical size of the weld zone could be compared to the micrographs of the weld cross-section obtained by an optical microscope, by which the accuracy of thermal analysis can be verified. The numerical model is then transferred to mechanical analysis module in ANSYS by switching the element type from thermal to structural. The corresponding constraints are exerted into sample boundaries. The achieved temperature histories are subsequently loaded into the mechanical model step by step to calculate the displacement, stress/strain of the sample due to the thermal expansion or shrinkage during the welding process. A bilinear hardening principle is introduced in this study to simulate the material plastic behavior. Von Mises criterion is used for considering the yield behavior of the sample material. Figure 5 shows the numerical procedure used in this study.

3. Experimental set-up

A 4 kW fiber laser and a GMAW torch are mounted on a robotic arm to perform the hybrid welding of a thick plate for a butt joint configuration. The photo of an experimental set-up for welding is shown in Figure 6. In order to control the gap thickness, spot welding is performed at both ends of the joint before the formal welding starts. After the welding process is completed, the achieved sample will be cut into standard tensile coupon for tensile test, the left parts will be mounted for polishing, and etching to test the micro-hardness and microstructure. The base metal is high strength steel A514; its chemical composition is listed in Table 1. The wire material is ER100S-G. Its diameter is 0.9 mm, and its chemical composition is listed in Table 2. Residual stresses were measured by using the X-ray diffraction technique. Before performing the residual stress measurement, the measurement areas were cleaned by using polishing paper.

	C	Mn	P	S	Si	Cr	Mo	V	Ti	B
Min.	0.12	0.70			0.20	0.40	0.15	0.03	0.01	0.0005
Max.	0.21	1.00	0.035	0.008*	0.35	0.65	0.25	0.08	0.04	0.005

Table 1. Chemical composition of A514 [61]

Cu % max	Ni % max	Fe % max	Mn % max	Mo % max
<0.5	<5.0	Balance	<5.0	0.50

Table 2. Chemical composition of ER100S-G [62]

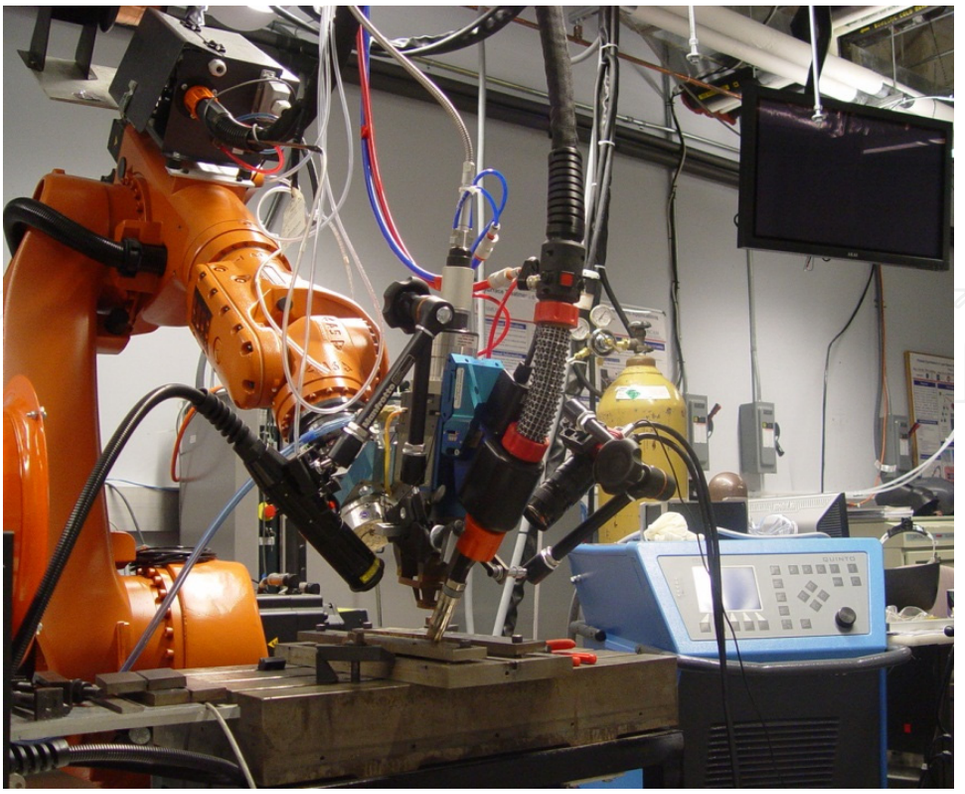

Figure 6. Photo of hybrid laser-GMA welding system used in this study

4. Results and discussion

4.1. Experimental results

Figure 7 shows the surface morphology of A514 weld obtained by hybrid laser-GMA welding, and Figure 8 presents the corresponding cross-sectional view of weld. It can be

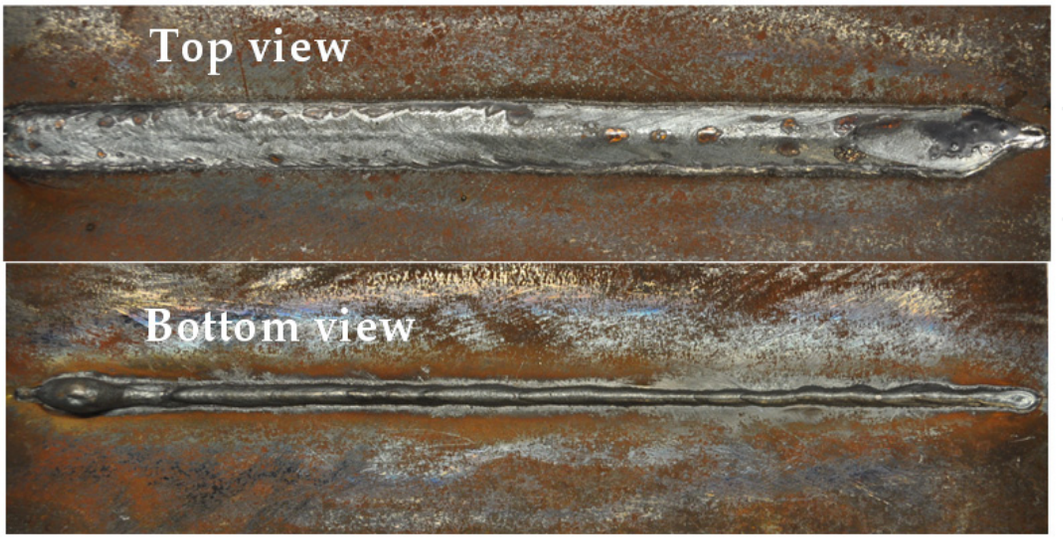

Figure 7. A514 sample achieved by 3.8 kW laser and 159A×30.5V GMAW with a welding speed of 12 mm/s and 8-mm stand-off distance between the laser and arc

seen that a sound weld quality is achieved by using hybrid laser-GMA welding and the welding-induced cracks can be effectively mitigated by reasonably selecting filler wire matched with base metal. Also, a sound mechanical property can be obtained. Figures 9a and b show the hardness distribution in the weld obtained by hybrid laser-GMA welding.

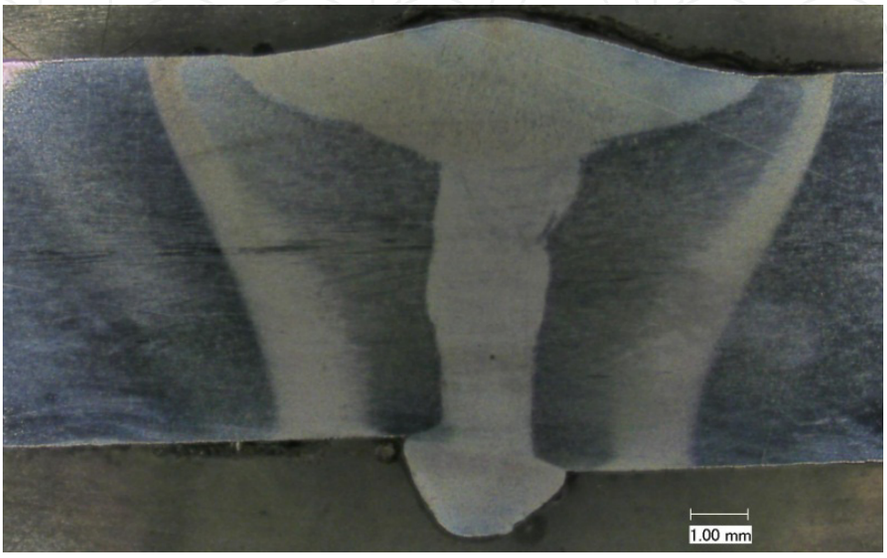

Figure 8. Cross-sectional view of A514 weld sample achieved by 3.8 kW laser and 159A×30.5V GMAW with a welding speed of 12 mm/s and 8-mm stand-off distance between the laser and arc

4.2. Thermal results and grain size prediction in the HAZ of hybrid laser-GMA welding

Finite element analyses results show the temperature at the each location of weld with respect to the welding time. The temperature evolution curves at position A, B, and C are shown in Figure 10, where position A is located at the center of weld, position B is at the heat-affected zone, and position C is in the base metal, as shown in Figure 11b. Figures 11a and b show the top and cross-sectional views of weld obtained by hybrid laser-GMA welding, respectively. It is inevitable that material heating and cooling is accompanied by phase transformation and grain size change, especially in the HAZ of weld, which is the weakest zone of the weld. In this study, a Monte Carlo-based sub-model is introduced to numerically predict the grain growth in the HAZ combined with the finite element thermal analysis. Figure 12a shows the relationship of temperature versus Monte Carlo step at Position B, and Figure 12b presents the curve of Monte Carlo step versus real time at Position B. The corresponding predicted grain size distribution in the Position B is shown in Figure 12c. The numerically predicted grain size is compared to grain size shown in the micrograph of the cross-section of weld (see Figure 12d), and a qualitative agreement is achieved.

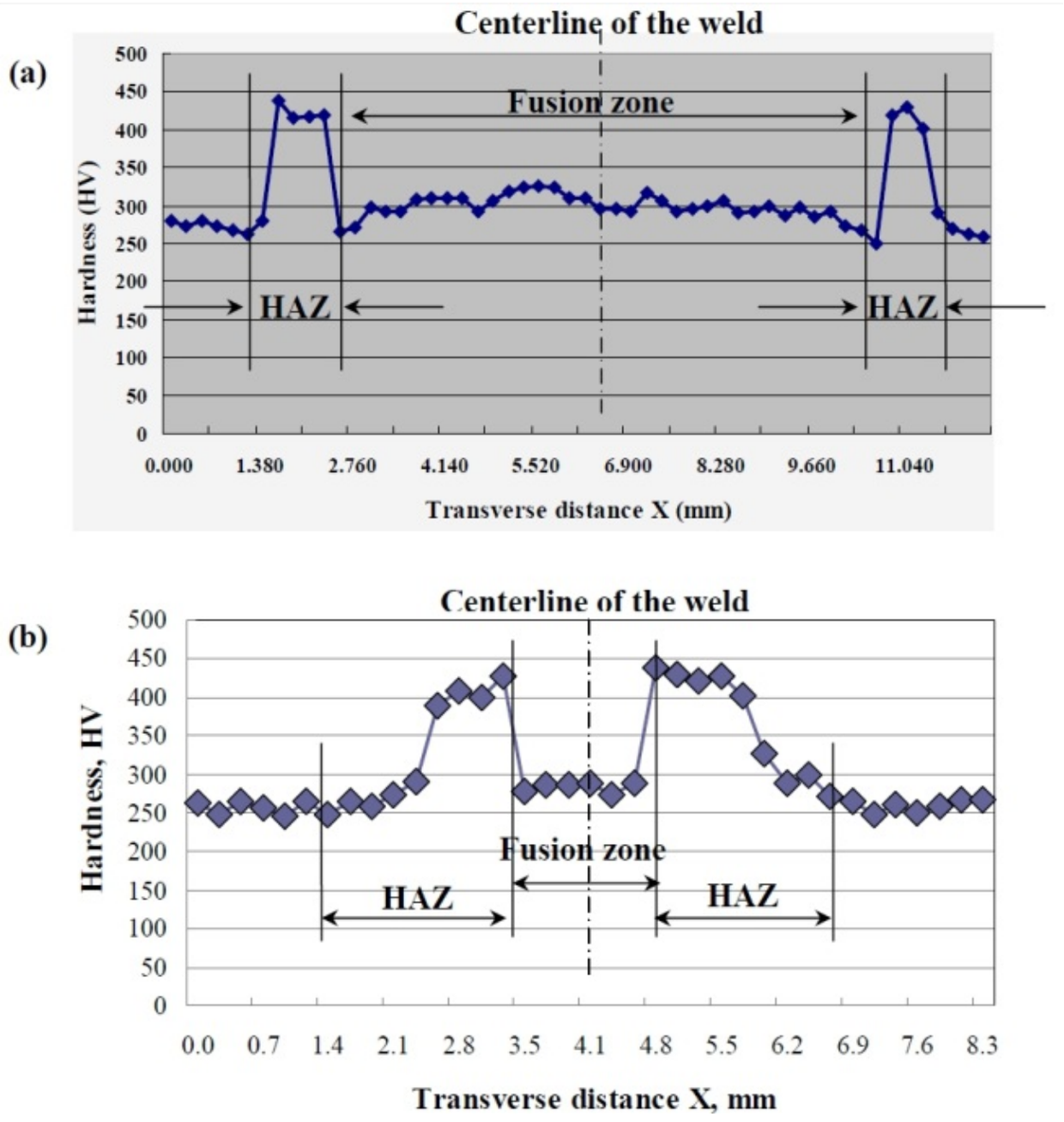

Figure 9. Hardness distribution transverse to the weld in A514 sample, (a) at the top surface and (b) at the bottom surface

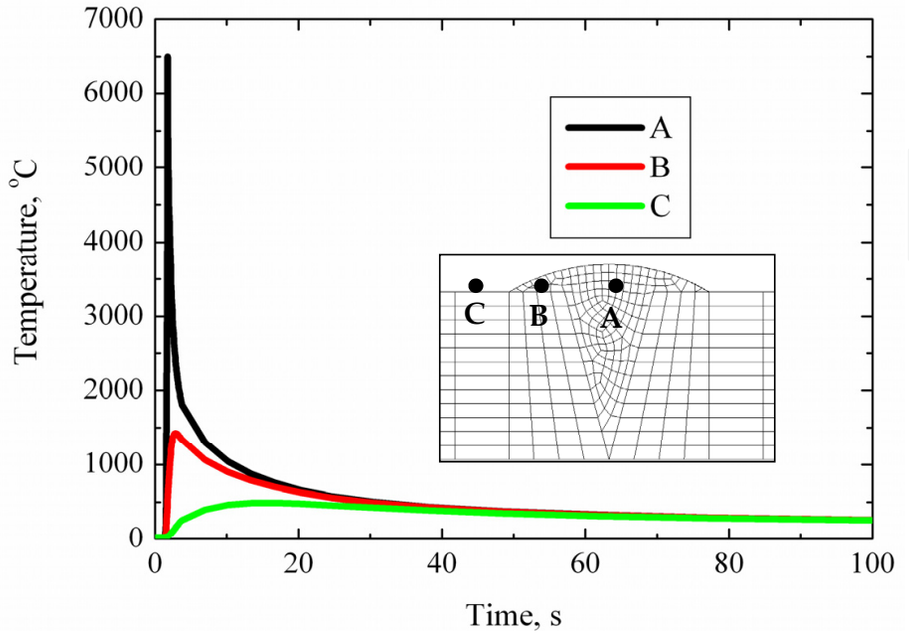

Figure 10. Temperature evolution curve at the FZ, HAZ and BM during the hybrid laser-GMA welding of A514 steel

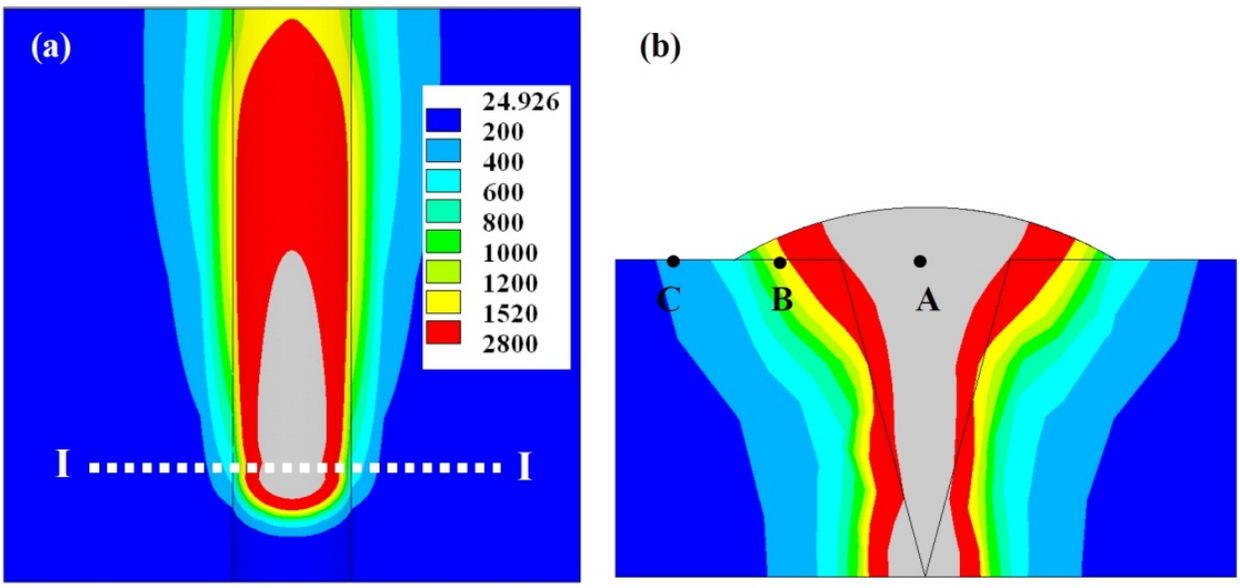

Figure 11. Numerically predicted isotherms at the top (a) and at the cross-section I-I of the weld (b) obtained by hybrid laser-GMA welding

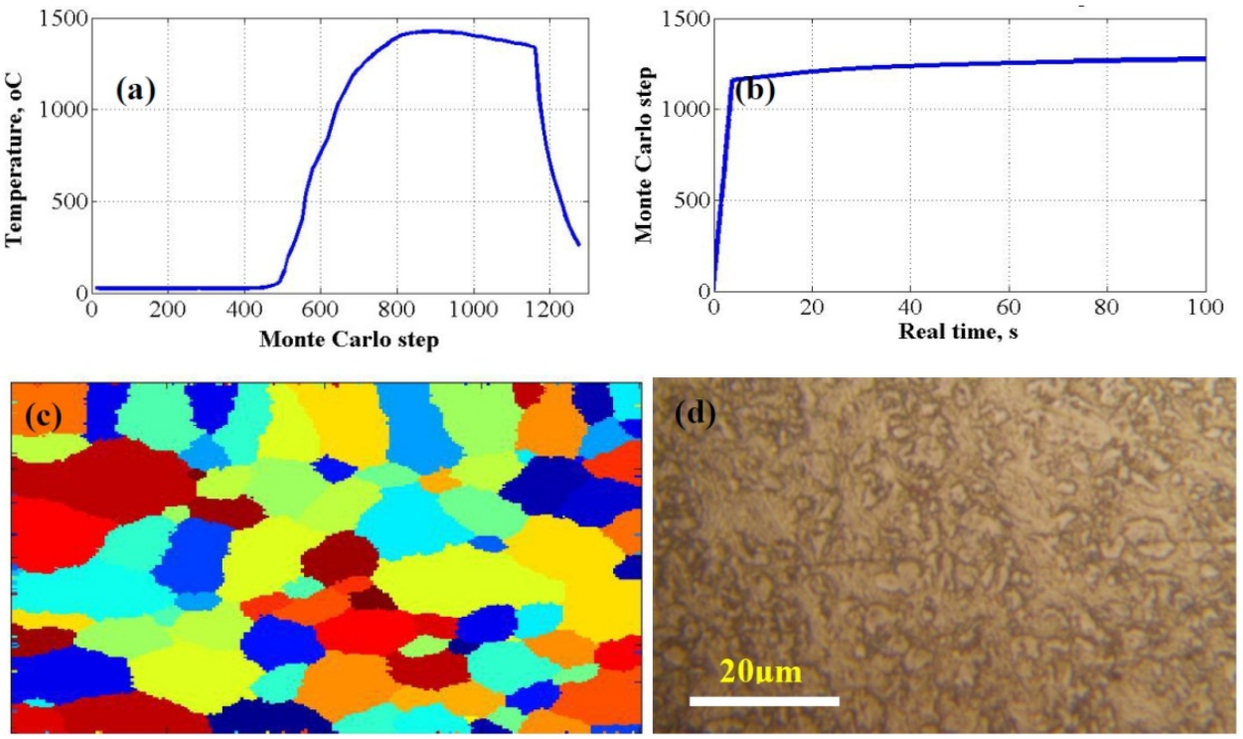

Figure 12. (a) Temperature versus Monte Carlo step, (b) Monte Carlo step versus real time, (c) numerical predicted and (d) experimentally measured grain size distributions at Position B in the HAZ of hybrid A514 weld by Monte Carlo sub-model

4.3. Thermally-induced residual stress in the hybrid laser-GMA welding

A finite element analysis is further performed to predict the thermally-induced residual stress distribution based on the previous thermal analysis results. The contours of transient stress, along thickness normal stress, longitudinal stress and equivalent residual stress of hybrid weld are shown in Figures 13a through d, respectively. It can be seen that the higher stress concentrations are located at the weld zone, which also indirectly verifies the previously experimentally obtained conclusions that the thermally induced cracks are usually generated at the weld zone, not in the base metal. The corresponding contours of stress distribution of the cross-section in the middle of weld length are shown in Figures 14a through d. A higher stress concentration is found to be located at the top region of cross-section

Figures 15a through c show residual stress distribution transverse to the weld bead at the different thicknesses in the middle of weld obtained by hybrid laser-GMA welding. It also validates the conclusion driven from Figure 14 that high tensile transverse and longitudinal stresses are located at the top and bottom regions of the weld center, high compressive transverse stresses are located at a half of the weld thickness. From the equivalent stress distribution point of view, the peak value of stress concentration is a little lower than that at the top and bottom of the weld. Figure 16 shows residual stress distribution transverse to the weld bead at the different locations along the top surface of weld obtained by hybrid laser-GMA welding. Figure 17 also shows residual stress distributions along the central line

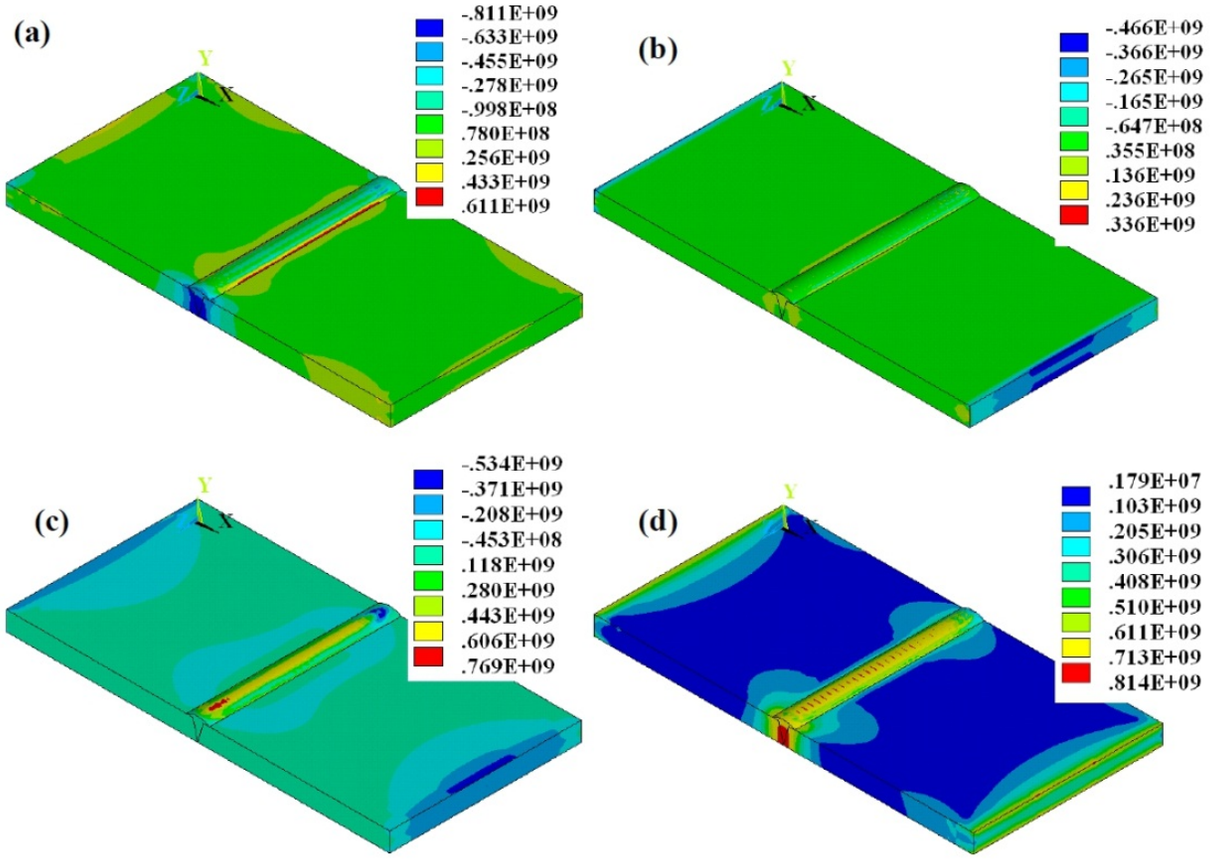

Figure 13. (a) Transverse stress SX, (b) along-thickness normal stress SY, (c) longitudinal stress SZ, and (d) von Mises equivalent residual stress SEQV mapping of weld by hybrid laser-GMA welding (unit of stress in the contour is Pa)

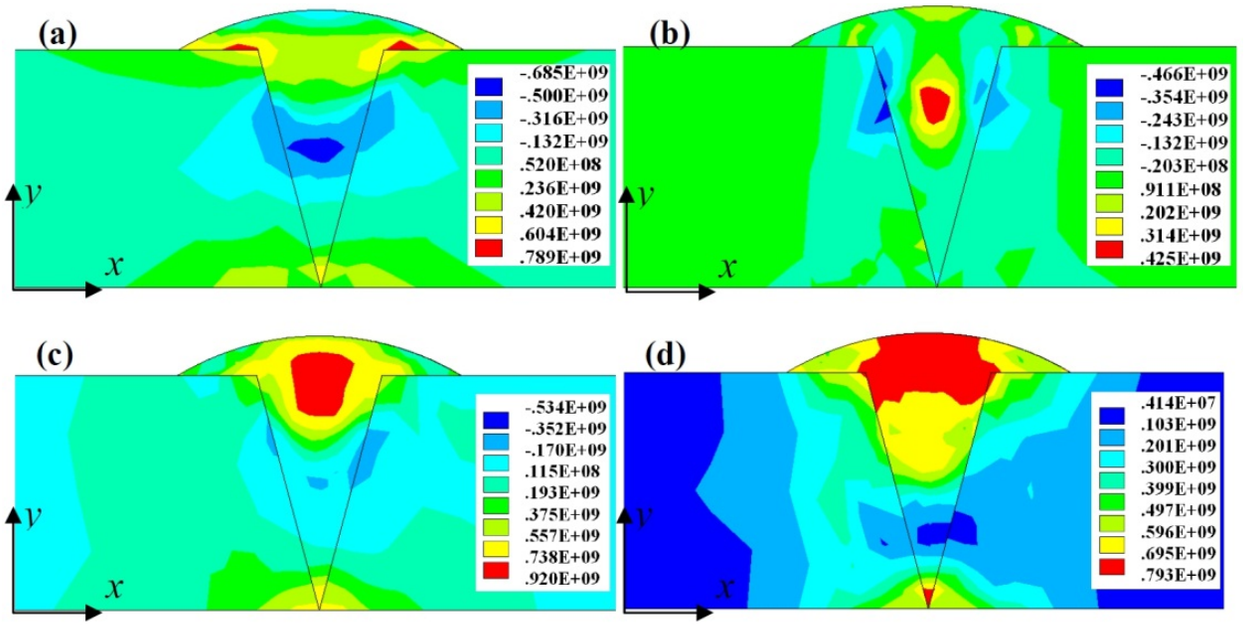

Figure 14. (a) Transverse stress SX, (b) along-thickness normal stress SY, (c) longitudinal stress SZ, and (d) von Mises equivalent residual stress SEQV mapping of cross-section of weld by hybrid laser-GMA welding (unit of stress in the contour is Pa)

at the top surface of weld centerline achieved by hybrid laser-GMA welding. It is clear that stress distribution across the weld bead is uniform along the weld; only a little drop in stress magnitude exists at the both ends of weld.

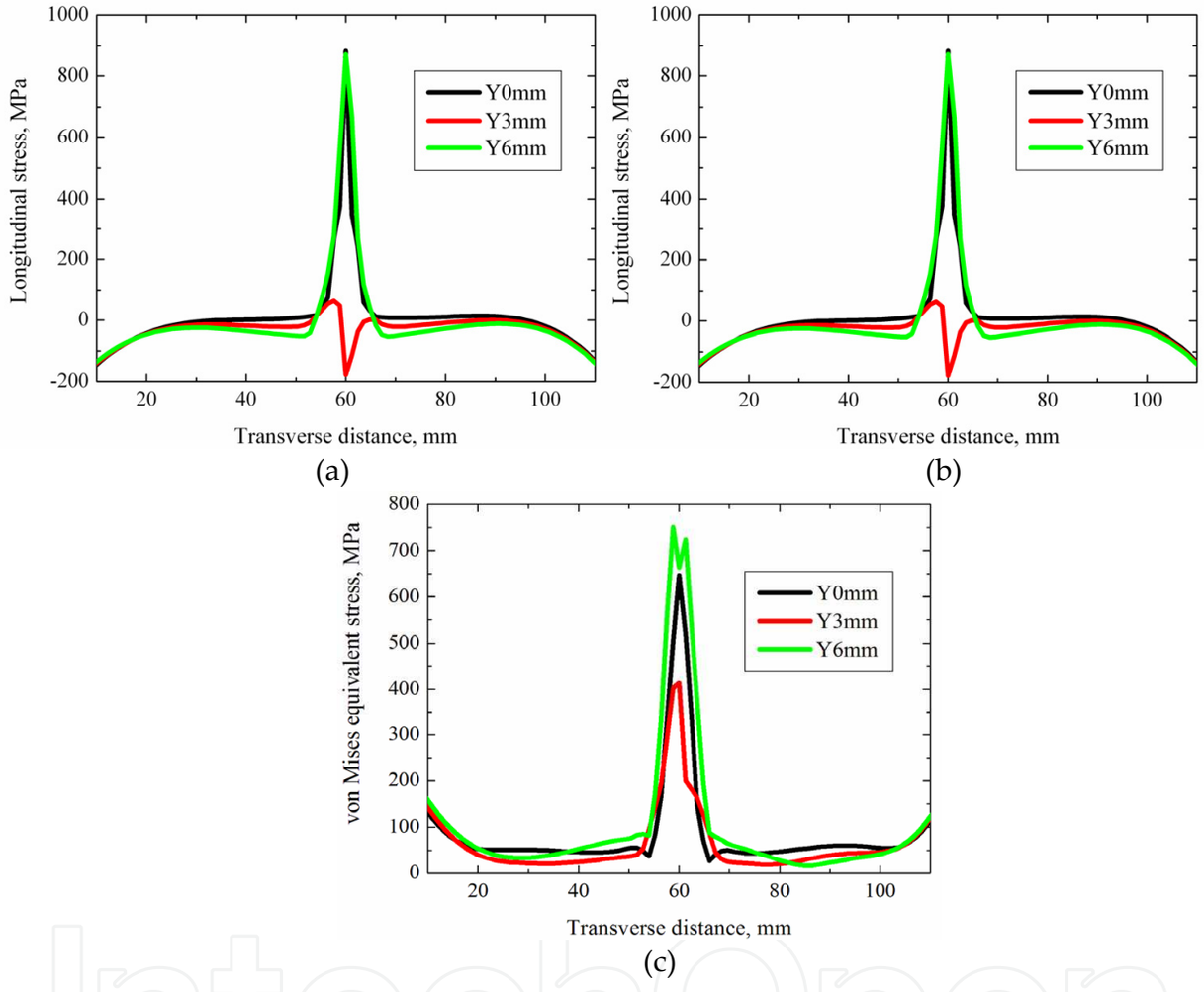

Figure 15. Residual stress distribution transverse to the weld bead at the different thicknesses in the middle of weld (z=30 mm) obtained by hybrid laser-GMA welding

Figure 18 shows a comparison of experimentally-measured and FE numerically-predicted residual stress distributions at the middle of weld length of top surface of weld by hybrid laser-GMA welding. There is a qualitative agreement between the developed numerical model and experimentally measured stress by an X-ray diffraction technique. Figures 19, 20 and 21 show the transverse, longitudinal, and equivalent stresses as well as temperature evolution with time at the positions A, B and C, respectively. It can be seen that the peak values of transient stresses at positions A, B, and C are sensitive to the temperature curve at the position A but not at the positions B and C.

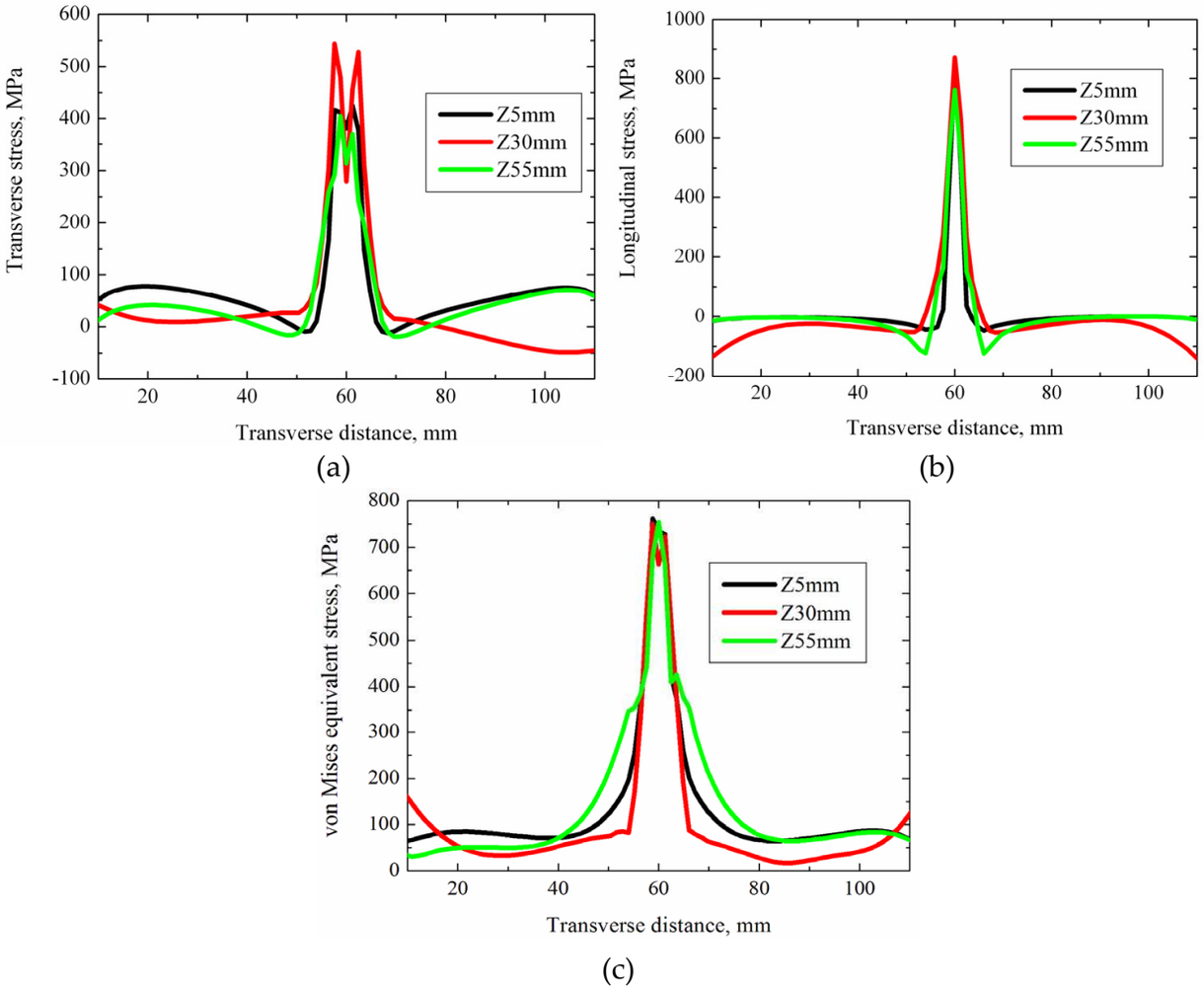

Figure 16. Residual stress distribution transverse to the weld bead at the different locations along the top surface of weld obtained by hybrid laser-GMA welding

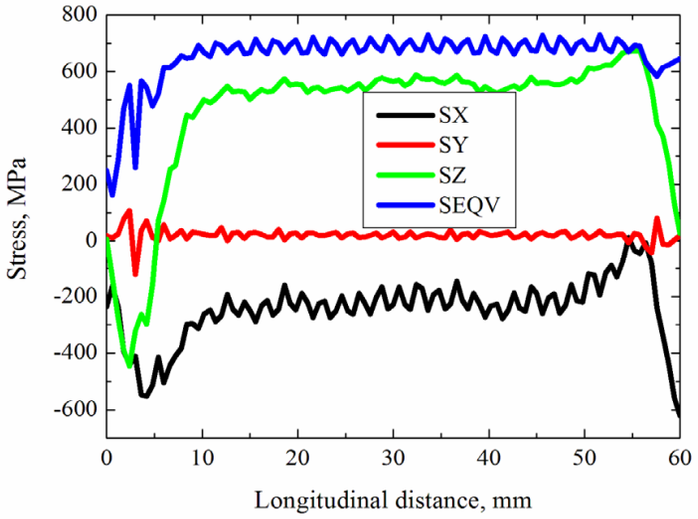

Figure 17. Residual stress distributions along the longitudinal direction of weld at the top surface of weld centerline achieved by hybrid laser-GMA welding

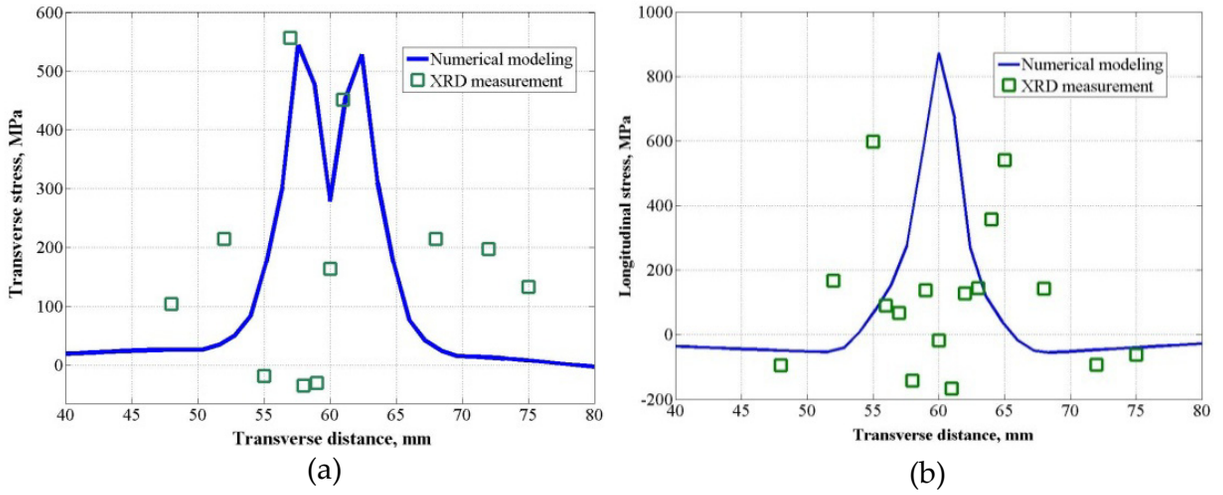

Figure 18. Comparison of experimentally-measured and FE numerically-predicted residual stress distribution at the middle of weld length of top surface of weld by hybrid laser-GMA welding

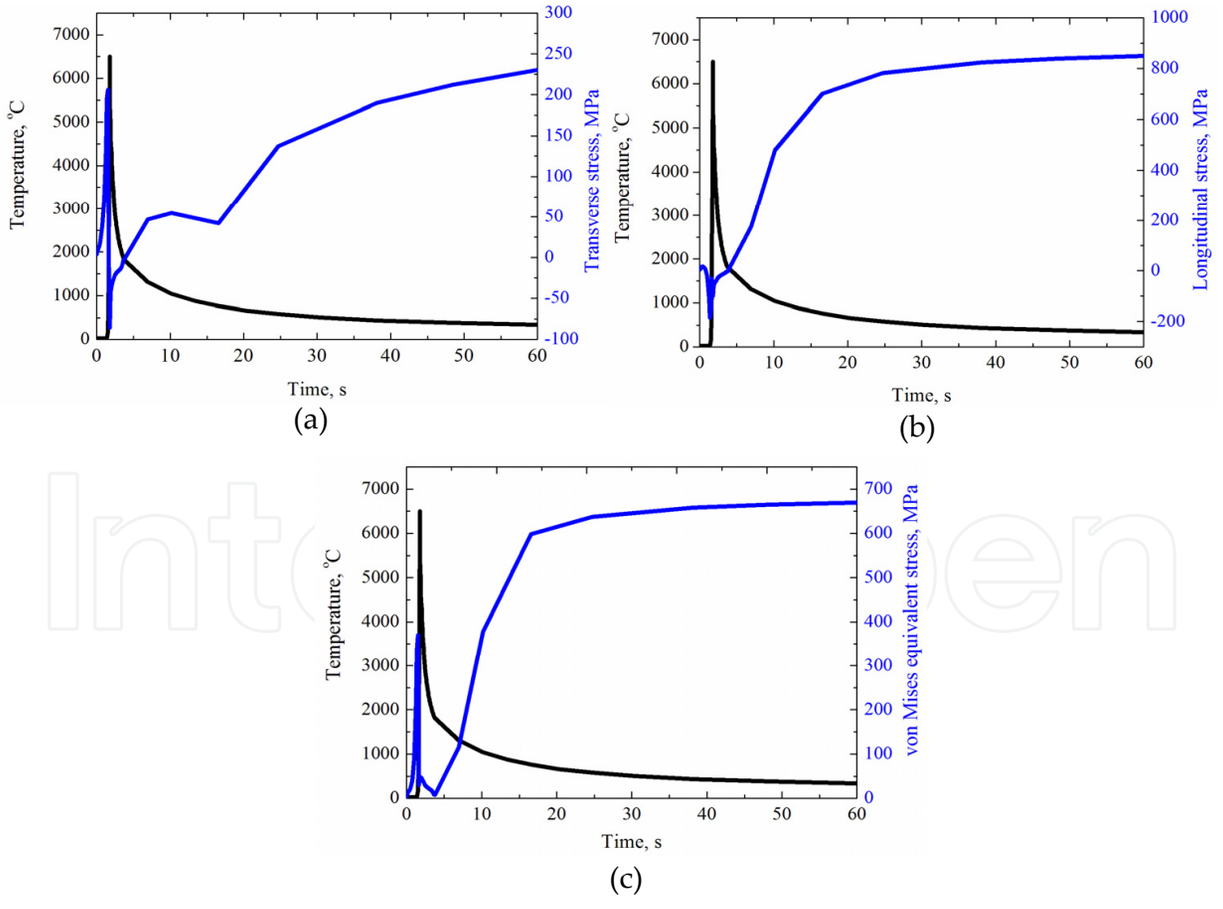

Figure 19. Stress and temperature evolution curves at the Position A in FZ of hybrid A514 weld

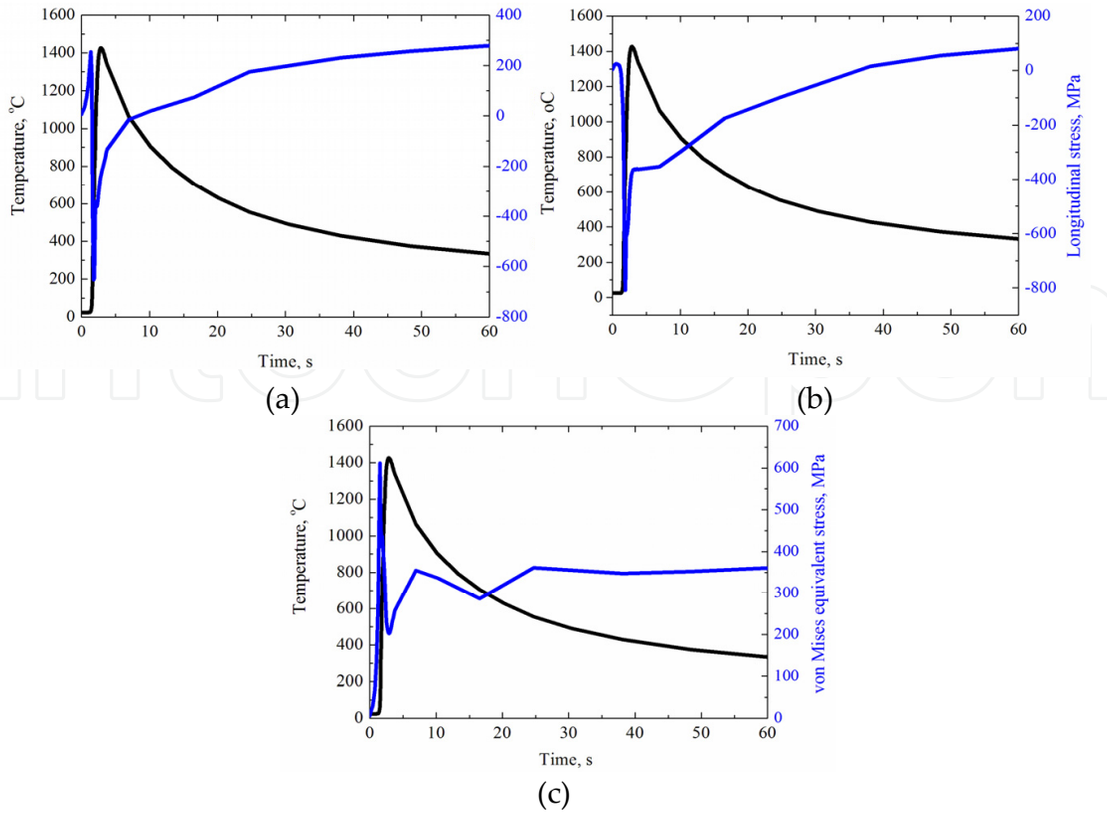

Figure 20. Stress and temperature evolution curves at the Position B in HAZ of hybrid A514 weld

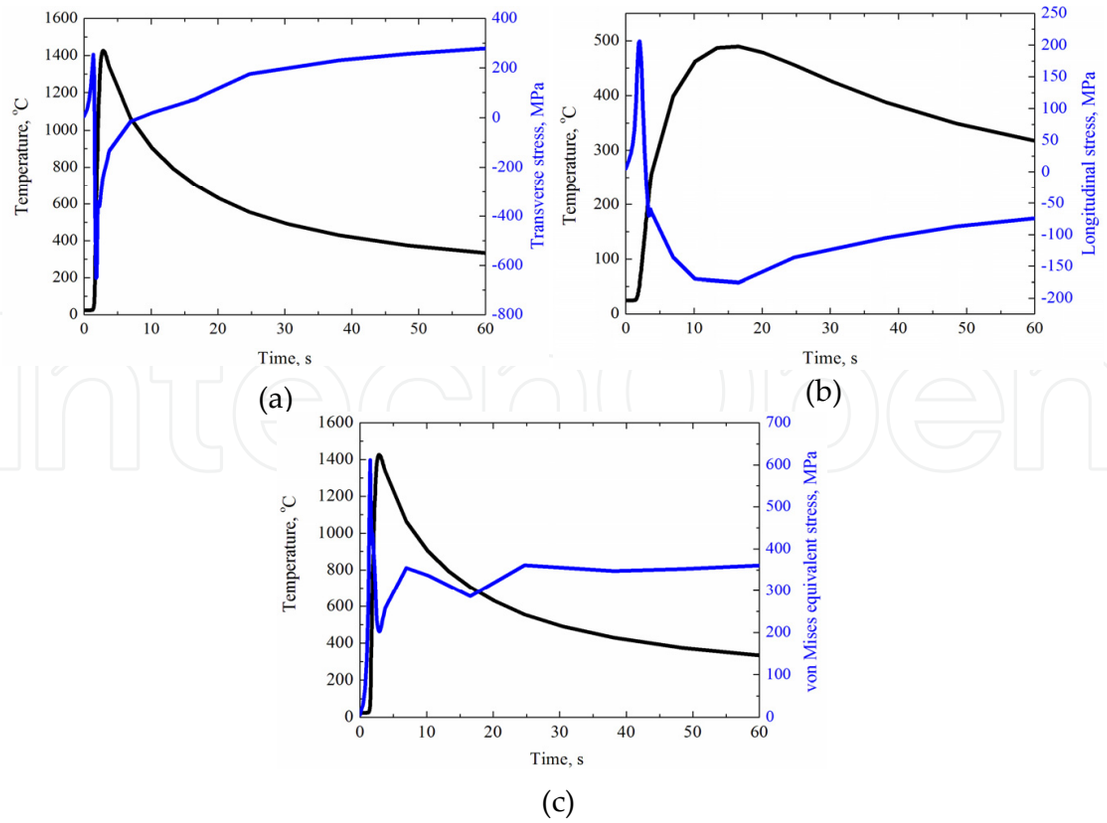

Figure 21. Stress and temperature evolution curves at the Position C in BM of hybrid A514 weld

5. Conclusions

The hybrid approach combining laser and arc has unique features which definitely help to achieve a better weld quality and to improve the production efficiency. A brief overview of modeling of hybrid laser-arc welding process has been presented in which heat transfer, fluid flow, residual stress and distortion, as well as phase transformation in the weld zone and heat affected zone, are involved. As a case study, a 3D thermo-mechanical finite element model is developed to study the thermally-induced residual stress in the hybrid laser-GMA welding process. A Monte Carlo model is introduced to numerically predict the grain growth in the heat affected zone of weld combined with finite element thermal analysis, which can be used to further understand the welding mechanisms of hybrid laser-GMA welding as well as other welding technology.

Author details

Fanrong Kong and Radovan Kovacevic*
Research Center for Advanced Manufacturing, Lyle School of Engineering, Southern Methodist University, Dallas, TX, USA

Acknowledgement

The authors would like to thank Ph.D. candidate, Mr. Junjie Ma for his valuable help in the experiment and technical discussions and Research Engineer, Mr. Andrew Socha for his support in the experimental set-up. This work was financially support by NSF's Grant No. IIP-1034652

6. References

[1] C. Roepke, S. Liu, S. Kelly, and R. Martukanitz. Hybrid laser arc welding process evaluation on DH36 and EH36 steel. Welding Journal, 2010, 89: 140s-150s.
[2] C. Bagger and F.W. Olsen. Review of laser hybrid welding. Journal of Laser Applications. 2005, 17(1): 2-14.
[3] M. N. James, D. J. Hughes, Z Chen, H Lombard, D. G. Hattingh, D. Asquith, J. R. Yates and P. J. Webster, Residual stresses and fatigue performance, Engineering Failure Analysis, 2007,14: 384-385.
[4] P. Kah. Usability of laser-arc hybrid welding processes in industrial applications. Ph.D. Dissertation, Lappeenranta University of Technology, 2011.
[5] G. Turichin, E. Valdaytseva, I. Tzibulsky, A. Lopota, O. Velichko. Simulation and technology of hybrid welding of thick steel parts with high power fiber laser. Physics Procedia, 2011, 12: 646-655.
[6] M.H. Cho and D.F. Farson. Simulation study of a hybrid process for the prevention of weld bead hump formation. Welding Journal, 2007, 86: 174s-179s.

* Corresponding Author

[7] F.G. Lu, S. Yao, S.N. Lou, Y.B. Li. Modeling and finite element analysis on GTAW arc and weld pool. Computational Materials Science, 2004, 29:371-378.
[8] H.G. Fan, H.L. Tsai, S.J. Na. Heat transfer and fluid flow in a partially or fully penetrated weld pool in gas tungsten arc welding. International Journal of Heat and Mass Transfer, 2001, 44: 417-428.
[9] H.J. Aval, S. Serajzadeh, A.H. Kokabi. Prediction of grain growth behavior in HAZ during gas tungsten arc welding of 304 stainless steel. Journal of Materials Engineering and Performance, 2009, 18: 1193-1200.
[10] L.J. Yang, M.J. Bibby, R.S. Chandel. Linear regression equations for modeling the submerged arc welding process. Journal of Materials Processing Technology, 1993, 39(1-2): 33-42.
[11] D. V. Kiran, B. Basu, A.K. Shah, S. Mishra, and A. De. Three-dimensional heat transfer analysis of two wire tandem submerged arc welding. ISIJ International, 2011, 51 (5): 793-798.
[12] J. Haidar. A theoretical model for gas metal arc welding and gas tungsten arc welding I. Journal of Applied Physics, 1998, 84: 3518-3529.
[13] J. Haidar. Prediction of metal droplet formation in gas metal arc welding II. Journal of Applied Physics, 1998, 84: 3530-3540.
[14] J. Haidar. An analysis of heat transfer and fume production in gas metal arc welding. III, Journal of Applied Physics, 1999, 85 3448-3459.
[15] Z.H. Rao, J. Hu, S.M. Liao, H.L. Tsai. Modeling of the transport phenomena in GMAW using argon-helium mixtures. Part I- The arc. International Journal of Heat and Mass Transfer, 2010, 53: 5707-5721.
[16] C. Heinze, C. Schwenk, M. Rethmeier. Numerical calculation of residual stress development of multi-pass gas metal arc welding. Journal of Constructional Steel Research, 2012, 72: 12-19.
[17] A. Kaplan. A model of deep penetration laser welding based on calculation of the keyhole profile. Journal of Physics D: Applied Physics, 1994, 27(9): 1805-1814.
[18] R. Spina, L. Tricarico, G. Basile, T. Sibillano. Thermo-mechanical modeling of laser welding of AA5083 sheets. Journal of Materials Processing Technology, 2007, 191: 215-219.
[19] A.P. Mackwood, R.C. Crafer. Thermal modeling of laser welding and related processes: a literature review. Optics & Laser Technology, 2005, 37: 99-115.
[20] P. Martinson, S. Daneshpour, M. Koçak, S. Riekehr, P. Staron. Residual stress analysis of laser spot welding of steel sheets. Materials & Design, 2009, 30(9): 3351-3359.
[21] W. Tan, N.S. Bailey, Y.C. Shin. A novel integrated model combining cellular automata and phase field methods for microstructure evolution during solidification of multi-component and multi-phase alloys. Computational Materials Science, 2011, 50: 2573-2585.
[22] K. Asim, J. Lee, and J. Pan. Failure mode of laser welds in lap-shear specimens of high strength low alloy (HSLA) steel sheets. Fatigue & Fracture of Engineering Materials & Structures. 2011, 35: 219-236.

[23] Y. Arai, M. Kikuchi, T. Watanabe, M. Nakagaki. Residual stress due to welding and its effect on the assessment of cracks near the weld interface. International Journal of Pressure Vessels and Piping. 1995, 63(3): 237-248.
[24] Y.P. Yang, P. Dong, J. Zhang and X. Tian. A hot-cracking mitigation technique for welding high-strength aluminum alloy. Welding Journal, 2000, 79(1): 9s-17s.
[25] A.H. Dilawari, T.W. Eagar and J. Szekely. An analysis of heat and fluid flow phenomena in electroslag welding. Welding Journal, 1978, 57(1): 24s-30s.
[26] L. A. Jones, T. W. Eager, J. H. Lang. Magnetic forces acting on molten drops in gas metal arc welding, Journal of Physics D: Applied Physics, 1998, 31: 93-106.
[27] P. Dong. Residual stress analyses of a multi-pass girth weld: 3-D special shell versus axisymmetric models. ASME Journal of Pressure Vessel Technology, 2001, 123: 207-213.
[28] P. Dong, J.K. Hong, and P. Rogers. Analysis of residual stresses in Al-Li repair welds and mitigation techniques, Welding Journal (London), 1998, 77 (11): 439-445.
[29] P. Dong, J.K. Hong, J. Zhang, P. Rogers, J. Bynum, and S. Shah, Effects of repair weld residual stresses on wide-panel specimens loaded in tension. ASME Journal of Pressure Vessel Technology, 1998, 120: 122–128.
[30] Dean Deng, Yu Luo, Hisashi Serizawa, Masakazu Shibahara, and Hidekazu Murakawa. Numerical simulation of residual stress and deformation considering phase transformation effect. Transactions of Joining and Welding Research Institute (Osaka University) 2003, 32(2): 325-333.
[31] D. Deng, H. Murakawa. Numerical simulation of temperature field and residual stress in multi-pass welds in stainless steel pipe and comparison with experimental measurements. Computational Materials Science, 2006, 37: 269-277.
[32] D. Deng. FEM prediction of welding residual stress and distortion in carbon steel considering phase transformation effects. Materials and Design, 2009, 30: 359-366.
[33] W.M. Steen, and M. Eboo. Arc augmented laser welding. Metal Construction, 1979, 11(7): 332-335.
[34] J. Zhou, H. L. Tsai. Modeling of transport phenomena in hybrid laser-MIG keyhole welding. International Journal of Heat and Mass Transfer, 2008, 51: 4353-4366.
[35] J. Hu, H.L. Tsai. Heat and mass transfer in gas metal arc welding. Part I: The arc. International Journal of Heat and Mass Transfer, 2007, 50 (5-6): 833-846.
[36] Z.H. Rao, S.M. Liao, and H.L. Tsai. Modelling of hybrid laser-GMA welding: review and challenges. Science and Technology of Welding and Joining, 2011, 16 (4): 300-305.
[37] B. Ribic, R. Rai, and T. DebRoy. Numerical simulation of heat transfer and fluid flow in GTA/laser hybrid welding. Science and Technology of Welding and Joining. 2008, 13 (9): 683-693.
[38] ANSYS Inc., ANSYS 11.0 Manual, 2007.
[39] S. Wu, H. Zhao, Y. Wang, X. Zhang. A new heat source model in numerical simulation of high energy beam welding. Transaction of China Welding Institute, 2004, 25: 91–94.
[40] V. Pavelic, R. Tanbakuchi, O.A. Uyehara, and P.S. Myers. Experimental and computed temperature histories in gas tungsten arc welding of thin plate, Welding Journal Research Supplement, 1969, 48: 259s-305s.

[41] E.A. Bonifaz. Finite element analysis of heat flow in single-pass arc welds. Welding research supplement, 2000, May: 121s-125s.
[42] J. Goldak, A. Chakravarti, and M. Bibby. A new finite element model for heat sources, Metallurgical Transaction B, 1984, 15B: 299-305.
[43] P. Peyffarth, and I.V. Krivt. Welding and Allied Processes Volume I. Laser-Arc Processes and Their Application in Welding and Material Treatment. Tailor&Francis, London, 2002.
[44] F. Kong, J. Ma, R. Kovacevic. Numerical and experimental study of thermally induced residual stress in the hybrid laser–GMA welding process. Journal of Materials Processing Technology, 2011, 211(6): 1102-1111.
[45] C.S. Wu, Q.X. Hu, J.Q. Gao. An adaptive heat source model for finite element analysis of keyhole plasma arc welding. Computational Materials Science. 2009, 46: 167-172.
[46] F. Kong, R. Kovacevic. 3D finite element modeling of the thermally induced residual stress in the hybrid laser/arc welding of lap joint. Journal of Materials Processing Technology, 2010, 210 (6-7): 941-950.
[47] M. Nosonovsky, X. Zhang, and S.K. Esche. Scaling of Monte Carlo simulation of grain growth in metals. Modelling and Simulation in Materials Science and Engineering, 2009, 17: 025004 (13pp).
[48] S.Mishra, T.Debroy. Measurements and Monte Carlo simulation of grain growth in the heat-affected zone of Ti-6Al-4V welds. Acta Materialia 2004, 52: 1183-1192.
[49] S.Sista, Z.Yang, and T. Debroy. Three-dimensional Monte Carlo simulation of grain growth in the heat-affected zone of a 2.25Cr-1Mo steel weld. Metallurgical and Materials Transactions B, 2000, Volume 31B: 529-536.
[50] F. Kong, S. Santhanakrishnan, D. Lin, and R. Kovacevic. Modeling of temperature field and grain growth of a dual-phase steel DP980 in direct diode laser heat treatment. Journal of Materials Processing Technology, 2009, 209 (18-19): 5996-6003.
[51] A. Farzadi, M Do-Quang, S. Serajzadeh, A.H. Kokabi, and G. Amberg. Phase field simulation of weld solidification microstructure in an Al-Cu alloy. Modelling and Simulation in Materials Science and Engineering, 2008, 16: 165005 (18pp).
[52] Ch.A. Grandin, J.L. Desbiolles, M. Rappaz, and Ph. Thevoz. A three-dimensional cellular automaton-finite element model for the prediction of solidification grain structures. Metallurgical and Materials Transaction A, 1999, 30A: 3153-3165.
[53] Dierk Raabe, Franz Roters, Frédéric Barlat, Long-Qing Chen, Continuum Scale Simulation of Engineering Materials: Fundamentals-Mcrostructures-Process Applications, Wiley-VCH, Weinheim, 2004.
[54] B. Radhakrishnan and T. Zacharia. Simulation of curvature-driven grain growth by using a modified monte carlo algorithm. Metallurgical and Materials Transactions A, 1996, 26(1): 167-180.
[55] S. Sista, Z. Yang, and T. Debroy, Three-dimensional Monte Carlo simulation of grain growth in the heat-affected zone of a 2.25Cr-1Mo steel weld, Metallurgical and Materials Transactions B, 2000, 31: 529-536.
[56] S. Mishra, T. Debroy, Measurements and Monte Carlo simulation of grain growth in the heat-affected zone of Ti-6Al-4V welds, Acta Materialia, 2004, 52: 1183-1192.

[57] Y.H. Wei, Y.L. Xu, Z.B. Dong, and J.L. Xia, Three dimensional Monte Carlo simulation of grain growth in HAZ of stainless steel SUS316, Key Engineering Materials, 2007, 353-358: 1923-1926.
[58] M.-Y.Li, E. Kannatey-Asibu, Monte Carlo simulation of heat-affected zone microstructure in laser-beam welded nickel sheet, Welding Journal, March 2002: 37-44.
[59] Weibin Wang, Yaowu Shi, Yongping Lei, and Zhiling Tian, FEM simulation on microstructure of DC flash butt welding for an ultra-fine grain steel, Journal of Materials Processing Technology, 2005,161: 497-503.
[60] J. H. Gao, R. G. Thompson, Real time-temperature models for Monte Carlo simulations of normal grain growth, Acta Materialia, 1996, 44: 4565-4575.
[61] http://www.ssab.com/Global/SSAB/SSAB_Americas/A514%20Grade%20S%20Brochure%2006-25-08.pdf
[62] http://www.midalloy.com/html/pdf/low_alloy/TB%20ER100S-G%20Weld.pdf